Journal of Applied Fluid Mechanics, Vol. 18, No. 3, pp. 756-768, 2025.
Available online at www.jafmonline.net, ISSN 1735-3572, EISSN 1735-3645.
https://doi.org/10.47176/jafm.18.3.2759

Investigation of Compressor Surge Process and Flow Field Details Using Numerical Simulation

Y. Qiao, W. Chu† , H. Zhang, K. Wang and X. Yang

School of Power and Energy, Northwestern Polytechnical University, Xi'an, Shaanxi, 710072, P. R. China

†*Corresponding Author Email: wlchu@nwpu.edu.cn*

ABSTRACT

Surge phenomenon is investigated for an axial compressor through a set of experiments. In addition, the full-annulus numerical simulation method is used to numerically simulate the surge phenomenon and analyze the flow field details during the surge process. The results identified four distinct stages in the surge: forward deceleration, reverse flow, forward recovery, and chamber recovery. The forward recovery stage, the flow field experiences stall with the occurrence of unevenly distributed stall regions. In contrast, the chamber recovery stage at the same flow rate exhibits a more uniform flow field without stall regions. These findings highlight the capability of the capability of the full-annulus calculation method to provide insights into the flow field details during the surge process. The information can serve as a reference for the development of accurate surge models and the study of the influence of surge on the internal flow of the compressor passage.

Article History

Received April 5, 2024
Revised August 28, 2024
Accepted September 21, 2024
Available online January 1, 2025

Keywords:

Axial compressor
Surge process
Flow field details
Full-annulus calculation
Numerical simulation

1. INTRODUCTION

The compressor is a vital component of an aero-engine. However, compressor surge is a self-excited periodic oscillation phenomenon that occurs during the operation of the compressor due to unstable airflow (Guo et al., 2023). Surge can cause serious consequences including reduced efficiency, increased noise, component damage, flame blow-out in the combustion chamber, burning the turbine, and even airplane crash accidents.

Research on compressor surge has a rich history. In early work (Greitzer, 1976a, b), the author conducted an experimental study on surge in a three-stage axial compressor, quantifying the system parameters during surge transients. In the theoretical research of surge, Crevel et al. (2014) proposed a method to analyze the mechanism and influence of rotating stall and surge in high-speed compressors, utilizing URANS simulation to calculate the surge process of compressors. Greitzer (2009) further contributed with a one-dimensional mathematical model of the axial compression system. Meanwhile, Modern research delves deeper. Some scholars continued to explore the surge mechanism in multi-stage compressors (Zhao et al., 2021), and Langston (2017) provides a comprehensive summary of stall and surge mechanisms, their influence, and control methods. (Wang et al., 2020) systematically investigated the impact of downstream system volume and average mass flow on surge characteristics. Shahriyari et al.(2024) compared the effectiveness of bifurcation and LQR (Linear–quadratic regulator) controller for two compressor post-stall models, namely MG and SK. Without the controller, both MG (Moore—Greitzer) and SK (a developed model based on MG by Shahriyari Khalegh) models can lead to instability when the disturbance amplitude is small and the initial operating point is located in the positive slope region of the compressor characteristic. When the LQR controller successfully activated both models.

Accurate prediction of surge is crucial. (Arroyo et al., 2021)established a full-engine CFD model to predict the occurrence of surge, while (Righi et al., 2020) proposed a new three-dimensional low-order surge model. Bitikofer et al. (2017) identified the model parameters using a parameter identification method based on the genetic algorithm in the Moore-Greitzer model, which enhanced the prediction accuracy of the model. Liu et al. (2015) proposed a method based on eigenvalue analysis to predict the onset of flow instability in high-speed axial compressors. Courtiade and Ottavy (2013) conducted a wind tunnel experiment, analyzing surge transients in detail. They identified several precursor phenomena that could be used for early surge detection, providing valuable insights for surge warning systems. Lee et al. (2018) proposed that the single-channel calculation strategy would lead to premature "numerical stall" in numerical calculation and prediction of surge, and the overall

NOMENCLATURE

B	number of criteria for judging unstable flow of compressor	U	circumferential velocity at the average radius of the compressor blade
A_C	interface area of the compressor	L_C	pipeline length
V_P	volume of the exhaust system	a	speed of sound
ρ	airflow density	ω	Lmholtz resonator frequency

calculation method can have a better correlation with the experiment. Based on the analysis of the working principles of fuzzy controller and expert controller, a fuzzy expert PID controller is designed (Yi & Sun, 2024). This controller has the advantages of both fuzzy control and expert control, such as good stability, high control accuracy, and fast response time. Their MATLAB simulation results show that the fuzzy expert PID control algorithm has the characteristics of high stability, fast response speed, and small overshoot compared with the traditional PID algorithm.

Research on surge control offers various approaches. (Schoenenborn & de Vries, 2013) established an aeroelastic model that reduced the surge load through deliberate tuning, paving the way for control methods. Munari et al. (2019), a coefficient is proposed: the surge severity coefficient. It can quantify the harmfulness of surge and be used to evaluate the harmfulness of different degrees of surge. Faltin and Beneda (2024) conducted a numerical study on the flow field and behavior of centrifugal compressors during surge with open and closed bleed valves. Their findings explored the design of injecting bleed air into the main flow path through the impeller blade passages to help centrifugal compressors operate at higher safety levels near unstable conditions. Xu et al. (2024) present a novel approach for controlling compressor system stall and surge instability using a finite-time backstepping-based adaptive sliding mode method. The most important innovation of this research is to provide a finite-time adaptive control approach to simultaneously prevent stall and surge instability in compressor systems with disturbances and uncertainties in the compressor characteristic curve and throttle valve. Guo et al. (2024) effectively improved the compressor instability margin by considering the uncertainty of compressor processing, and avoided the occurrence of surge phenomenon within a certain range. Zhang et al. (2024) aim to further reduce the adverse effects of tip leakage vortex by miniaturization using circumferentially equidistant through-holes on the casing. A novel passive unsteady flow control method is established for micro centrifugal compressors. This method takes full advantage of the unsteady characteristics of the flow field. The coherent structures of the tip leakage vortex are numerically investigated using dynamic mode decomposition. The numerical results are then applied to the physical system. The experimental test results of the system show that the improved flow control method can improve the maximum efficiency and surge margin of the compressor by 2.5% to 9.0%, respectively, and it can also improve the maximum pressure ratio.

Research on high-speed compressor surge and recovery is a complex yet continuously evolving field. With the deepening of research, people's understanding of surge deepens, and the technology of surge prediction, control, and recovery has also become more mature. At the same time, data-driven machine learning and artificial neural networks (ANNs) are increasingly playing a role in compressor surge research. Sheng et al. (2020) propose an active surge control method using a wavelet neural network algorithm, which has the property of approximating any linear and nonlinear function, to asymptotically approximate the unknown steady-state characteristics of the compressor. Then, by backstepping the second-order MG compressor surge dynamic model with CCV (close-coupled valve), a robust adaptive active controller for compressor surge is designed, which greatly improves its tracking and anti-surge performance. Zheng et al. (2021) developed a data standardization preprocessing algorithm based on batch sliding window (DSPABSW) and optimized the aero-engine surge fault detection fusion neural network (ASFDFNN) to improve the detection accuracy of aero-engine surge faults. Finally, the effect of detecting aero-engine surge faults 260 ms in advance is achieved. Hou et al. (2022) addressed early surge detection and diagnosis (ESDD) in centrifugal compressors using an adaptive feature fusion and sparse ensemble learning approach based on bearing vibration signals.

During the occurrence of surge, the occurrence of stall is not always accompanied by surge, and the flow field distribution types vary at different stages of the surge process. Moreover, the coupling between stall phenomenon and surge phenomenon in different stages of surge results in differences in its flow field, as the experiment can only observe the compressor surge performance macroscopically rather than accurately capturing the changes in the small flow field.

Based on the surge test of a subsonic axial compressor test rig, this paper adopts the method of numerical simulation for numerical calculation. The strong correlation between numerical calculation and experimental data allows for a detailed analysis of the flow field and the various state mechanisms involved in the surge process. Meanwhile, the experimental results show that the surge process is accompanied by stall. This phenomenon has been discovered in previous studies (Amulfi et al., 1998), but its mechanism has not been explored. In this paper, the stall phenomenon during the surge process is analyzed in detail based on the numerical analysis results verified by experimental results.

2. RESEARCH OBJECT AND METHOD

2.1 Research Object

This study investigates the first-stage rotor and stator blades of a single-stage axial compressor test rig at

Fig. 1 Photograph of the test rig

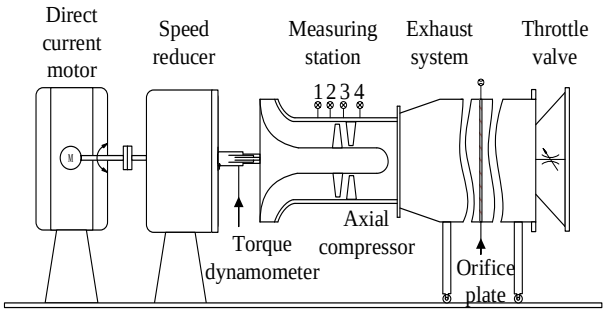

Fig. 2 Schematic diagram of the test rig

Northwestern Polytechnical University. The main components of the test rig include a 315KW direct current motor, a speed increaser whose transmission ratio of the accelerator is 15:1, a torque dynamometer, a radial inlet, an axial compressor test section, an exhaust system, a discharge section with orifice plates, and an automatically controlled movable cone throttle valve. Visual representations of the test rig are provided in Fig. 1 and 2: Fig. 1 shows a photograph of the test rig which shows the scale of the test rig by the door of the observation room, while Fig. 2 offers a schematic diagram.

Table 1 summarizes the design and aerodynamic parameters of the test rig used for the study.

The corresponding computational model is illustrated in Fig. 3. It consists of six key components: an inlet, a chamber 1, a rotor, a stator, a chamber 2, and an outlet.

The inclusion of chamber 1 addresses two critical challenges: flow recirculation and pressure pulsation at the inlet, which can lead to calculation divergence. To accurately capture compressor stall characteristics, a large chamber 2 is incorporated at the outlet. This chamber simulates the ambient atmosphere by specifying the total temperature and total pressure at the inlet enabling effective numerical analysis of the stall process. Chamber 2 is set to match the actual compressor volume from the experiment. Finally, a throttling cone-shaped outlet wall is implemented to accurately represent the real environment. The analysis process utilizes 30 rotor blades and 44 stator blades within the model.

Table 1 Design and aerodynamic parameters of the test rig

Parameter	Value
design flow rate (kg/s)	5.6
design isentropic efficiency	0.905
design pressure ratio	1.245
design rotational speed (rpm)	15200
tip relative Mach number	0.78
hub ratio	0.61
casing inner diameter (mm)	298
blade tip clearance (mm)	0.3
rotor blade number	30

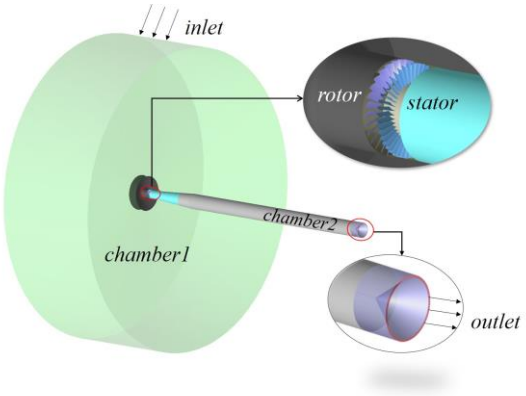

Fig. 3 Computational model

2.2 Numerical Method

The IGG-AutoGrid5 module within NUMECA software was used to generate the meshes for this numerical study. For the rotor mesh, the H-O-H topology was used for the fluid domain mesh within the channel, with O-type meshes surrounding the blades. The H-type topology was used for the inlet and outlet extension sections, and the "butterfly mesh" was used for the tip gap. The stator mesh was generated using the O4H topology. Figure 4 presents a schematic diagram of the grid generation for the rotor and stator. Additionally, to achieve high accuracy, the mesh was refined near the wall, resulting in a final $y+ < 2$. Full-annulus numerical simulation was employed for the calculations, utilizing a total mesh count of approximately 13.7 million.

The full-annulus calculation is employed to capture the comprehensive flow field information. Compared with single-passage calculation, the full-annulus calculation can simulate the flow field inside the entire passage, including the main flow region, boundary layer, and blade gap region. This enables the capturing of the interaction between the main flow region and the boundary layer, as well as the flow details inside the blade gap, such as flow separation and vortex structure. Moreover, full-annulus

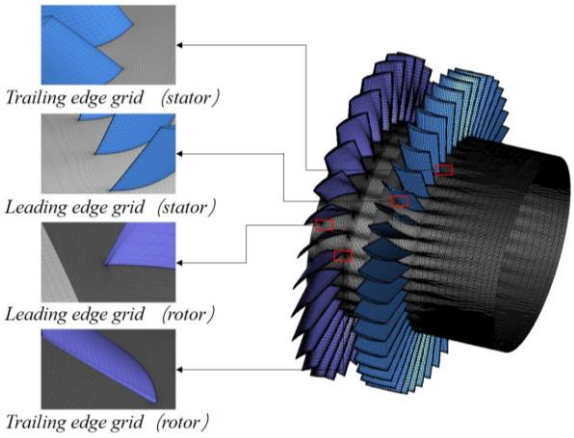

Fig. 4 Mesh division of the blade part

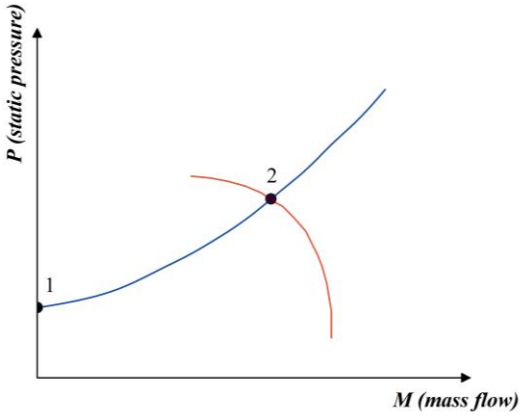

Fig. 6 Characteristic curve of a compressor

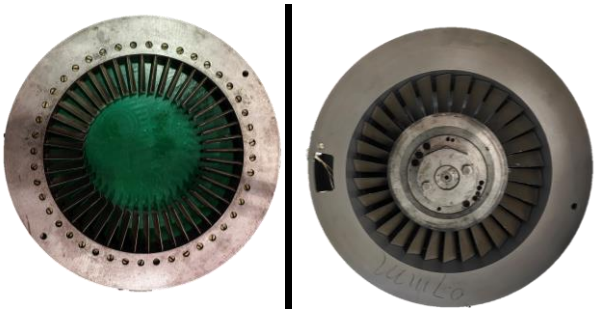

Fig. 5 Experimental parts of the rotor and stator

calculation can obtain the interaction between the fluids in different passages, which is crucial for studying surge occurrence and development. Figure 4 and 5 visually represent the mesh division of the blade part, and the experimental parts of the rotor and stator, respectively.

In this paper, the numerical simulation of three-dimensional time-averaged Navier-Stokes equations is carried out using NUMECA software in the calculation process. The calculation process is divided into two stages: steady calculation and unsteady calculation. The finite volume method with a central difference format is employed for the initial steady calculation stage, and to capture the time-dependent behavior, the explicit fourth-order Runge-Kutta method is used for time advancement in the unsteady calculation stage. Additionally, the multi-grid method and local time-stepping technology are implemented to accelerate the convergence of the solution.

The unsteady calculation stage leverages the k-epsilon (Low Re Yang-shih) turbulence model to account for turbulence effects.

To achieve a balance between computational efficiency and accuracy, a physical time step of 300 microseconds each period and a virtual time step of 20 are chosen. In unsteady solutions, the domain scaling method is used for all interfaces.

Between the calculations of different working conditions, the calculation results of the previous working condition are used as the initial conditions of the next working condition to improve the calculation efficiency and accuracy.

In terms of the setting of inlet and outlet boundary conditions, under steady-state conditions, the stall point is determined by iteratively decreasing the outlet static pressure while maintaining fixed inlet total temperature and total pressure. Different from the previous steady-state approach using a throttle valve model, this study employs Riemann Invariant boundary conditions for the unsteady calculations of the stall point and the flutter process.

Riemann Invariant boundary conditions offer several advantages when dealing with near-stall (The definition of near stall point during calculation is within 200Pa of the stall back pressure difference) and flutter regions in compressor simulations. Unlike traditional methods, they eliminate the need to choose between imposing pressure and mass flow rate at the boundary. Additionally, they avoid the use of a throttle valve model, which can introduce complexities in modeling the relationship between exit flow rate and static pressure.

Riemann Invariant boundary conditions require a straightforward characteristic curve to be defined by three parameters: target exit mass flow rate q_m, target exit pressure p_m (point 2 in Fig. 6), and pressure p_0 at zero mass flow rate (point 1 in Fig. 6). Based on these three parameters, a simple parabolic curve will be generated. Then, this curve is used to impose the boundary condition, thus establishing the relationship between mass flow rate and exit pressure.

The numerical calculation process is summarized in the flowchart present in Fig. 7. It consists of the following key steps: Establish a physical model, Mesh generation for numerical computation, Solve the governing equations, and Post-processing.

2.3 Numerical Verification

Leveraging the aforementioned numerical calculation method,this study performs a numerical simulation of the axial compressor and compares the results of the steady-state operating process with the corresponding experimental data. Figures 8 and 9 present the comparison of pressure ratio and efficiency curves as a function of flow rate, respectively.

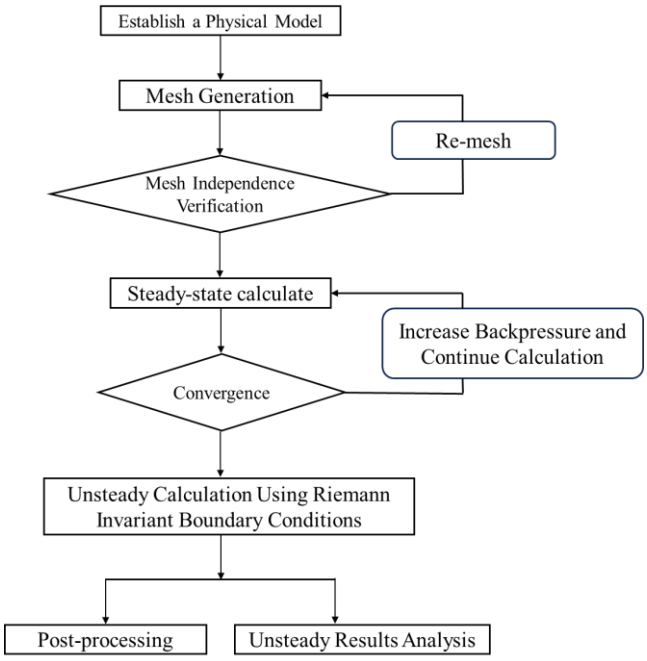

Fig. 7 flowchart of the numerical calculation

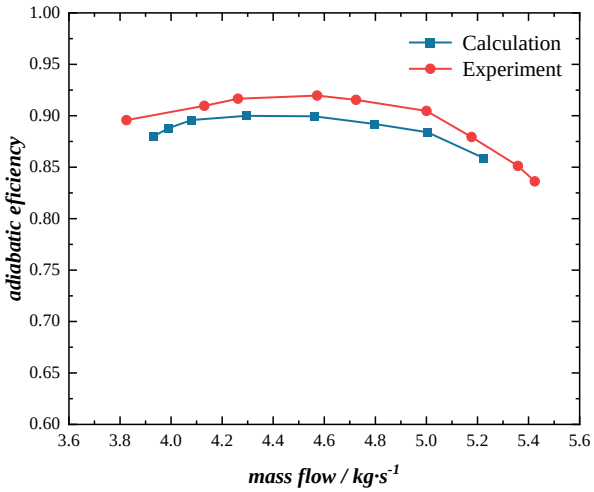

Fig. 8 Total pressure ratio characteristic curve

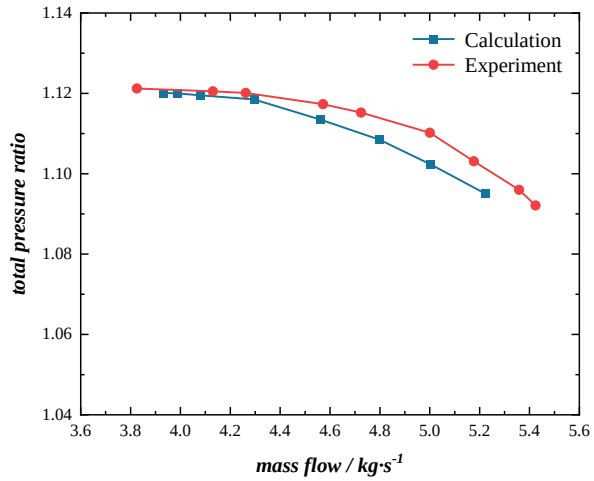

Fig. 9 Adiabatic efficiency characteristic curve

The analysis of the numerical results reveals the following key findings:

a. Consistent trends: The trends of pressure ratio and adiabatic efficiency curves obtained from the numerical calculations exhibit trends that closely match the experimental results. This consistency demonstrates the effectiveness of the numerical method in simulating the steady-state behavior of the test rig.

b. Error analysis: The errors between the numerical calculation and experimental results for pressure ratio and adiabatic efficiency are within 0.8% and 1.8%, respectively. These small errors indicate the high accuracy of the employed numerical calculation method.

3. RESULTS AND ANALYSIS

3.1 Basic Characteristics of Surge Ring

To process the surge numerical simulation, it is crucial to first verify whether the established compressor model can exhibit surge behavior. Extensive research has been conducted on compressor stability, including studies by E.M. Greitzer, who investigated the stability of compressors within piping and throttle systems. In his research on surge, the B-value judgment method is mostly used for analysis, and the judgment method of B-value is as shown in Equations (1),(2), and(3) (Greitzer, 1976a,b).

$$B = \frac{\frac{1}{2}\rho U^2 A_C}{\rho \omega U L_C A_C} \tag{1}$$

where

$$\omega = a\sqrt{\frac{A_C}{V_p L_C}} \tag{2}$$

thus

$$B = \frac{U}{2a}\sqrt{\frac{V_p}{A_C L_C}} \tag{3}$$

In the equation, L_C and A_C are the pipeline length and interface of the compressor respectively. Vp is the volume of the exhaust system, U is the circumferential velocity at the average radius of the compressor blade, and a is the speed of sound.

From equation (1), it can be seen that the numerator is proportional to the pressure difference across the compressor, which represents the driving force for accelerating the fluid in the compressor duct. The denominator is proportional to the inertial force of the fluid. Therefore, the B value actually represents the ratio of the driving force to the inertial force. As speed increases, the driving force grows more rapidly than the inertial force, so the working state of the compression system tends to surge.

Research suggests that each compressor has a specific B-value. When the B-value exceeds Bcr, the unstable flow phenomenon surge. Conversely, when the B-value is less than Bcr, only the rotating stall occurs without full surge. In this study, with a speed of 10765rpm, chamber 2 volume of 1.5m³, and a characteristic length is 8m, the calculated B-value is 0.947.

To further explore the stability characteristics of the single-stage compressor, experiments were conducted at

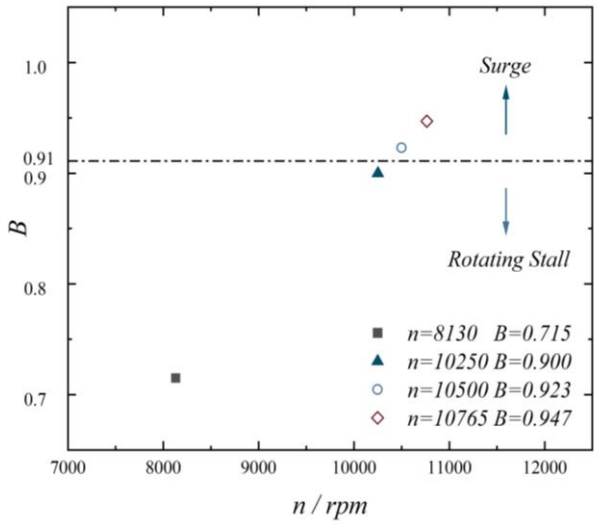

Fig. 10 Unstable flow types under different conditions

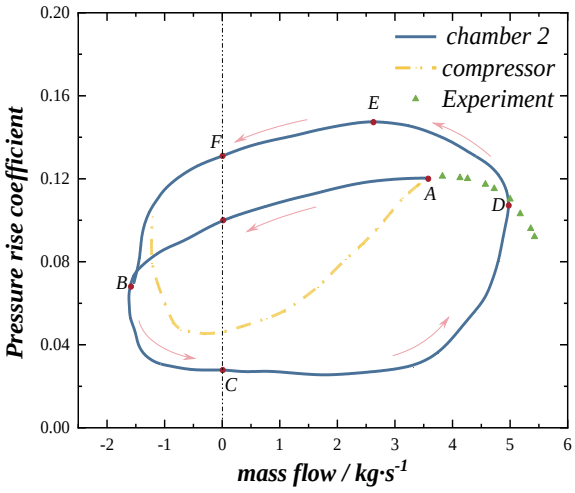

Fig. 11 Compressor transient pressure rise curve

various speeds and flow rates. The experimental results are shown in Fig. 10.

At the same time, experiments were carried out at n=9130rmp B=0.715, n=10250rmp B=0.900, n=10500rmp B=0.923, and n=10765rmp B=0.947. As the speed increased to 10500 rpm, a distinct change in the system's unstable mode occurred. The airflow exhibited axial, low-frequency oscillation accompanied by a "humming" sound, indicative of a surge state. Obviously, the compression system was in a surge state. When the speed was further increased, the unstable working mode of the system was still surge.

Figure 10 highlights the varying representative types of unstable flow observed across different operating conditions. The results demonstrate that the compressor speed, exhaust system structure, and size have a strong influence on the unstable working state of the compression system. Instability manifests differently at varying speeds and configurations.

By comparing the two unstable modes at n=10250rpm and n=10500rpm, it can be confirmed that the bifurcation point of the single-stage compression system is between 10250rpm and 10500rpm. Based on the experimental judgment criteria, it can be judged that the chosen physical model and speed conditions in the numerical calculations are confirmed to be capable of reducing surge.

In the numerical simulation of the compressor surge process, the unsteady calculation is first carried out under the near-stall condition (flow rate of 3.82kg/s). To achieve this, the Riemann Invariant boundary condition is employed for the calculation at the outlet. Figure 11 accurately depicts the compressor and chamber 2 pressure rise curves with flow rate change and the compressor characteristic map obtained from the experiment at steady state, which is used to describe the pressure rise and flow rate change in the compressor and chamber 2 during the surge event more clearly.

Figure 11 shows the curves of pressure rise with flow rate at different positions. The experiment represents the pressure ratio curve of the steady-state test compressor, the compressor represents the change of pressure rise with flow rate at the outlet of the compressor rotor, and chamber 2 represents the change of pressure rise with flow rate at the outlet of pipeline 2. The surge ring shown in Fig. 11 diagram reveals the dynamics of the surge phenomenon. When chamber 2 pressure exceeds the compression capacity of the compressor, the compressor flow rate will gradually decrease, which will lead to the surge and backflow of the compressor. As the flow velocity of the air at the inlet becomes the maximum negative value, the back pressure decreases, and the flow rate decreases with the back pressure. Subsequently, the flow rate becomes positive again, and the pressure in chamber 2 gradually recovers. However, once the pressure recovers to a value greater than the compression capacity of the compressor, the compressor flow rate decreases again and backflows, which leads to the cycle of engine surge.

To further illustrate the characteristics of the surge cycle, Fig. 12 presents the variation curve of the chamber 2 inlet flow. Figure 12 clearly shows that the flow

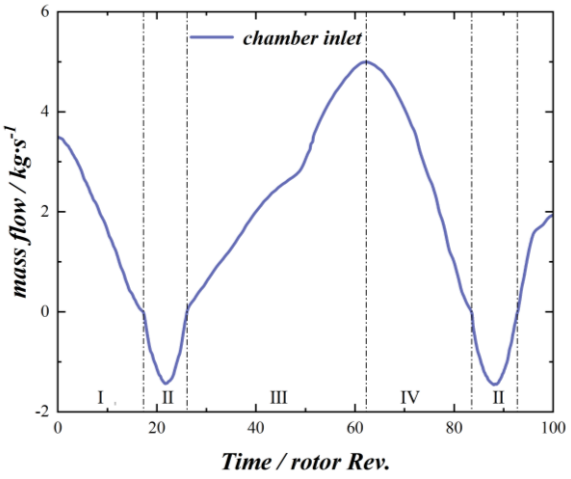

Fig. 12 Flow oscillation curve over time

undergoes significant amplitude changes during the surge process of the compressor. The maximum positive flow can reach 4.98*kg/s*, and the maximum negative flow is -1.46*kg/s*. The horizontal axis of Fig. 12 represents the number of rotations of the compressor rotor. According to the speed conversion, this phenomenon occurs at a frequency of 4.1 Hz.

For the purpose of better analyzing the different states in the surge process, the surge ring in Figure 10 is divided into four stages: forward deceleration (*AB*), reverse backflow (*BC*), forward recovery (*CD*), and chamber recovery (*DE*).

I. Forward Deceleration *(AB)*

In the initial phase of the surge process, the pressure in chamber 2 gradually decreases, and the flow rate of the compressor also slowly decreases.

This occurs because the compressor's pressure rise capability is insufficient to overcome the external pressure acting on it. Consequently, driven by the pressure differential, the flow rate within chamber 2 gradually decreases to zero from 3.82 kg/s. Subsequently, the flow rate continues to decrease from zero to -1.46 kg/s, and the rate of decrease increases, causing the backflow of the fluid in the channel, and eventually the negative value of the decreasing flow rate.

The axial velocity of the channel section at 20% chord length after the stator at the operating conditions of points A and B is analyzed, as illustrated in Figs 13 and 14.

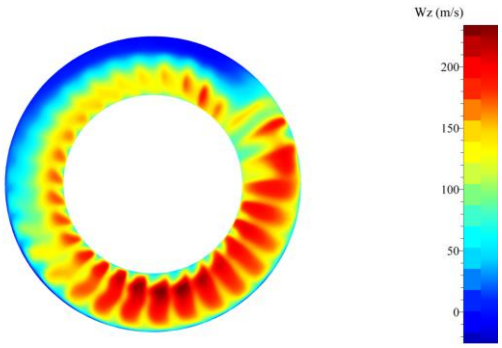

Fig. 13 Axial velocity distribution of the channel at the operating condition of point A

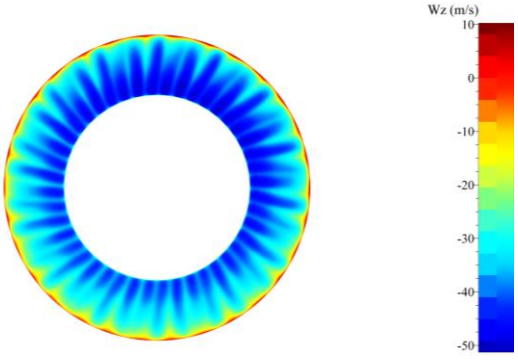

Fig. 14 Axial velocity distribution of the channel at the operating condition of point B

Figure 13 shows that a large amount of high-speed positive flow is unevenly distributed in the channels at the beginning of the surge process. This occurs because the compressor has just transitioned from a near-stall condition to a full surge state, resulting in an uneven circumferential distribution of the fluid in the channel.

As can be seen from Fig. 14, the axial velocity component of the fluid in the channel is negative at this time, and most of the flow is in the negative direction. The high-speed negative flow is concentrated from the blade root up to 80% of the blade height. This phenomenon occurs because, during the flow reversal process, the fluid near the casing has a reverse viscous resistance of equal value between the fluid layers at different blade heights due to the viscosity of the fluid.

This leads to a velocity gradient between the fluids at different distances from the casing, and eventually, the flow direction of the fluid near the casing remains in the positive direction.

II. Reverse Backflow *(BC)*

The occurrence of backflow signifies that the pressure in chamber 2 decreases and can on longer maintain a larger backflow rate. At a result, the backflow velocity is gradually decreasing, but backflow still occurs during this stage.

The flow rate in the compressor continues to decrease, and the pressure in the chamber continues to decrease, with the pressure rise droping sharply until the backflow rate decreases to zero. This marks the transition to the next stage of the surge process.

To investigate the phenomenon that the maximum backflow rate is reached at point B during the backflow process and then the backflow velocity decreases gradually afterward, the gap leakage flow at the working condition of point B is analyzed. Figure 15 illustrates the gap leakage flow lines at the working condition of point B.

During the backflow process, the gap leakage flow plays a crucial role in influencing the pressure distribution and velocity field of the backflow region. Consequently, it also affects the backflow rate and velocity.

As illustrated in Fig. 15, the gap leakage flow is primarily concentrated within the channel, and at this time

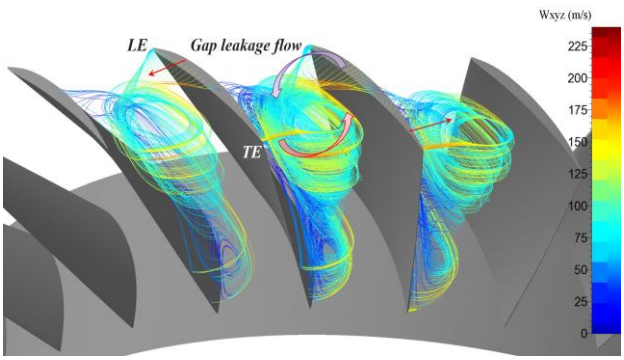

Fig. 15 Gap Leakage Flow Distribution at Point B

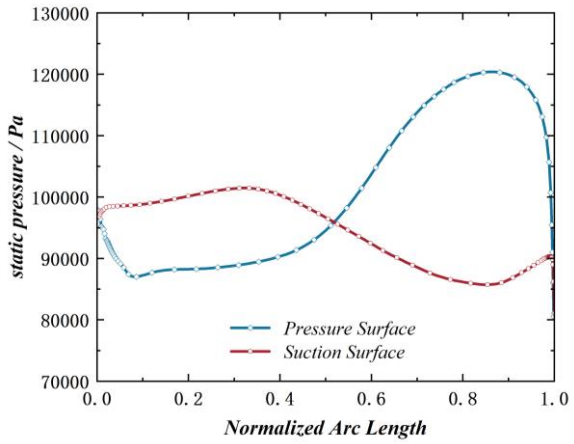

Fig. 16 Static Pressure Distribution of Suction and Pressure Surfaces at Point B

a phenomenon is found: in the blade tip gap leakage flow, the gap leakage flow near the leading edge of the blade flows from the suction surface to the pressure surface, and the gap leakage flow near the trailing edge of the blade flows from the pressure surface to the suction surface. The two parts of the vortex merge in the channel to form a single vortex that occupies the entire channel.

To investigate the reason behind the varying directions of the gap leakage flow at different blade chord lengths, static pressure variation parameters along the chord length of the blade suction surface and pressure surface are extracted as shown in Fig. 16.

The graph clearly reveals that at the position near the leading edge of the blade, the static pressure on the suction surface is greater than that on the pressure surface; at the same time, at the position of the trailing edge of the blade, the static pressure on the pressure surface is greater than that on the suction surface.

This explains the reason for the different directions of the gap leakage flow at different chord lengths. Furthermore, Fig. 15 highlights the information that the trailing edge of the gap leakage vortex forms turbulence. This part of the low-speed fluid flows around and enters the next channel, which blocks the movement velocity of the backflow, and then the backflow velocity gradually decreases.

Therefore, it can be understood that the reason for the different directions of the gap leakage flow at different blade chord lengths may be related to the difference in static pressure distribution and the formation of the gap leakage vortex. These factors collectively influence the fluid motion and velocity distribution during the backflow process.

III. Forward Recovery *(CD)*

As the surge process transitions from negative flow to positive flow, the compressor regains its pressure rise capability. During this stage, the compressor works normally, replenishes the gas in chamber 2, and increases the pressure of chamber 2. At the same time, with the recovery of the pressure rise capability, the flow rate in the channel gradually rises to a peak value of 4.98 *kg/s*.

In this process, literature (Amulfi et al., 1998) mentions the existence of a stall region in this process. Here, the energy loss of the flow field in this process is analyzed. In the loss analysis, the dissipation function (Φ) is used as a measure. The physical reason for this parameter is the entropy production caused by the shear action caused by the viscosity of the fluid during the fluid motion. The calculation formula is as follows:

$$\Phi = \mu\left[2\left(\frac{\partial V_x}{\partial x}\right)^2 + 2\left(\frac{\partial V_y}{\partial y}\right)^2 + 2\left(\frac{\partial V_z}{\partial x}\right)^2 + \left(\frac{\partial V_y}{\partial x} + \frac{\partial V_z}{\partial y}\right)^2 + \left(\frac{\partial V_x}{\partial y} + \frac{\partial V_y}{\partial z}\right)^2 + \left(\frac{\partial V_x}{\partial z} + \frac{\partial V_x}{\partial x}\right)^2\right] - \frac{2}{3}\mu\left(\frac{\partial V_x}{\partial x} + \frac{\partial V_y}{\partial y} + \frac{\partial V_x}{\partial z}\right)^2 \quad (4)$$

The cross sections at 50% span of the moving blades at points C and D are selected for analysis. Due to the high magnitude of Φ, logarithmic processing is applied to the value obtained at points C and D. The resulting cloud maps depicted the dissipation function are presented in Figs 17 and 18.

A comparison of Figures 17 and 18 shows that the dissipation function Φ at point D is significantly higher than that at point C. At the same time, the values under the two working conditions are averaged by flow rate, and the average values under the two working conditions are lgC(Φ)=6.4 and lgD(Φ)=7.2, with lgD(Φ) exceeding

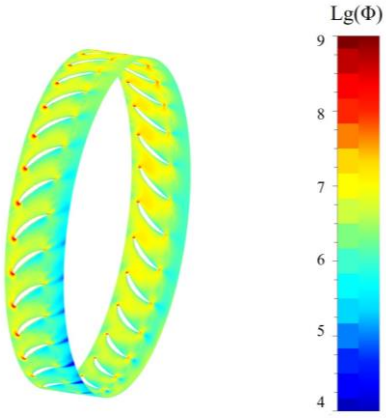

Fig. 17 lg (Φ) distribution cloud map of C

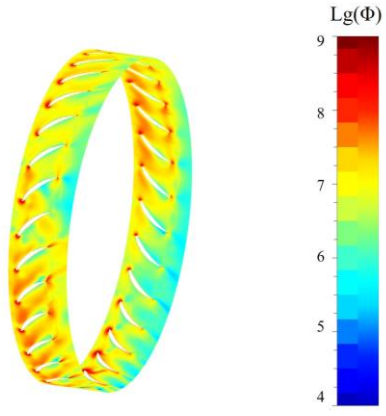

Fig. 18 lg (Φ) distribution cloud map of D

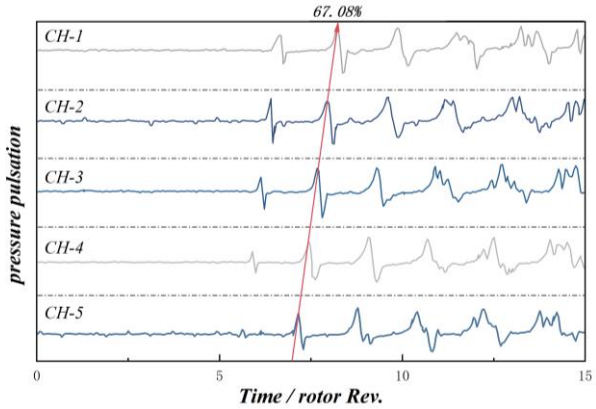

Fig. 19 Experimental curves of static pressure in different channels

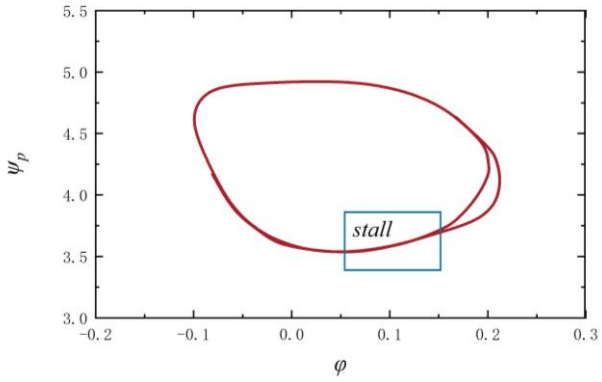

Fig. 20 Stalled portion of the surge cycle (Amulfi et al., 1998)

lgC(Φ). Macroscopically, it can be found that the loss at point D must be greater than that at point C. To investigate the specific reasons for this, an analysis is conducted on a smaller scale. The specific reasons for this difference in energy loss will be investigated in detail in Section 3.2.

IV. Chamber Recovery *(DE)*

At the end of the previous state, the compressor flow rate reaches its peak value, and the gradually increasing pressure within chamber 2 starts to limit the pressure rise capability of the compressor. The compressor's work capacity and flow rate decrease. When the compressor pressure rises and reaches its peak, the flow rate continues to decrease until it reaches state F. Subsequently, the compressor flow rate backflows again enters state II and continues numerical calculation. It's important to note that the pressure rise characteristic of the compressor overlaps with the first backflow process as the flow rate changes. In simpler terms, as the compressor enters surge, the pressure rise characteristic curve will move counter-clockwise along the surge loop.

3.2 Analysis of Stall Characteristics During Surge

During the surge process of the aero-engine, a phenomenon known as stall occurs within the flow path. These two phenomena are inherently coupled. The uneven flow field in the flow path caused by the movement of the stall cell will promote the occurrence of surge. At the same time, the changes in flow and pressure fluctuations caused by surge can influence the propagation and development of rotating stall cells.

The surge experiment conducted on the compressor in this study utilized a measuring point to capture the static pressure variation over time. Figure 19 presents this data. As evident from the figure, according to the time difference of pressure pulsation in different channels and the phase difference between channels. the static pressure exhibits significant fluctuations during the surge process. Calculations based on this data reveal that the stall cell movement speed within the flow path is approximately 67.08% of the engine speed.

According to Figure 20, the flow circumferential distribution within the channel exhibits relative uniformity during the chamber recovery process (process IV). Conversely, during the positive recovery process, the

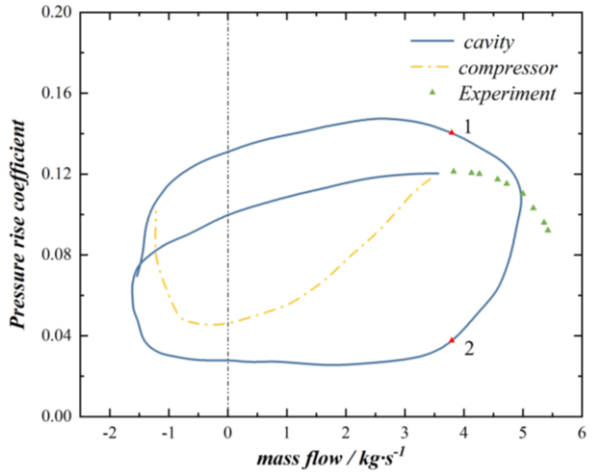

Fig. 21 Positions of points 1 and 2 on the surge loop

distribution in the channel is uneven and there are stall cells. This phenomenon has been documented in the literature (Amulfi et al., 1998), but a universally accepted explanation for this experimental observation remains elusive.

Because the experimental measurement methods are not sufficient to accurately measure the process of surge accompanied by stall phenomenon, the literature did not provide a reasonable explanation and solution suggestions for this phenomenon after elaborating on it.

During surge, two operating points 1 and 2 are chosen with the same mass flow on the surge loop, which are located in the chamber recovery*(DE)* and forward recovery*(CD)*, , as shown in Fig. 21.

The Mach number distributions at 98% blade height for the two operating conditions are depicted in Figs 22 and 23.

Figures 22 and 23 show the flow field distributions under two different conditions, respectively. By comparing the two figures, we can find the following obvious differences:

1. Uniformity of flow field distribution

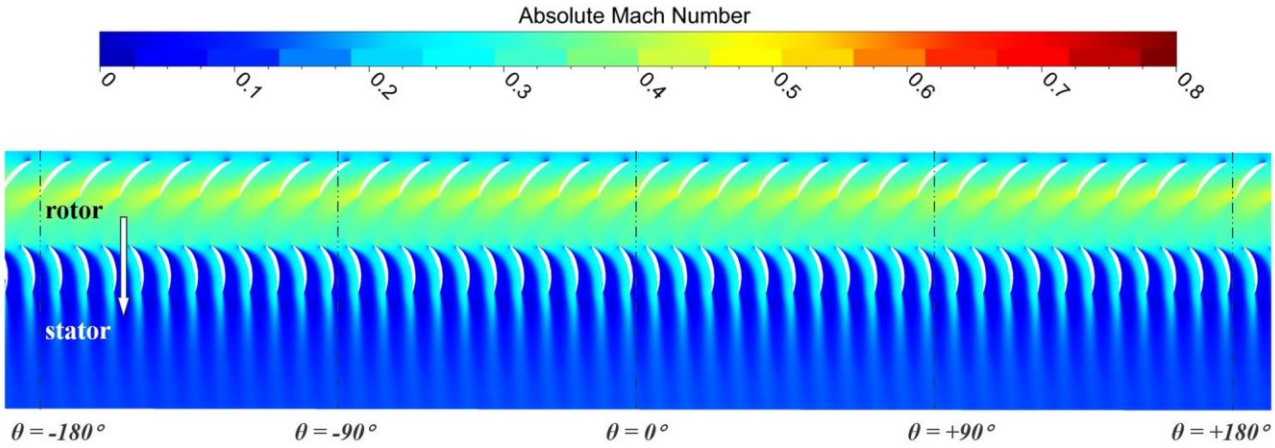

Fig. 22 Mach number distributions at 98% of blade height at point 1

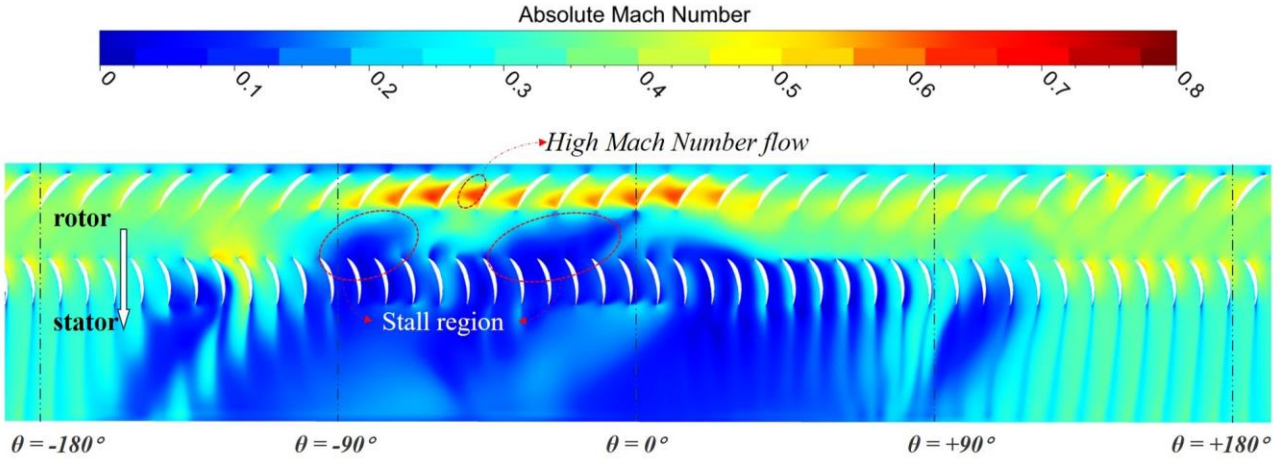

Fig. 23 Mach number distributions at 98% of blade height at point 2

In Fig. 22, the flow field at point 1 exhibits a uniform distribution, with no discernible evidence of flow separation or vortex phenomena.

In Fig. 23, a rotating stall region is present in the flow field at point 2, and the flow field distribution is uneven. A stall region is a region where the fluid velocity decreases to zero or near zero, leading to flow instability and even flow separation.

2. Mach number distribution

In Fig. 22, the Mach number distribution across different channels appears relatively uniform, with minimal variation.

In Fig. 23, the Mach number distribution across different channels varies, and the flow field distribution between channels is uneven. Mach number is a crucial parameter used to characterize the flow velocity within the flow field. The uneven distribution of the Mach number indicates that the flow velocities in different channels are different, potentially leading to flow instability.

3. Consistency between numerical calculation and experimental results

At the same time, we arranged measurement points in different channels in numerical calculations and obtained that the propagation speed of the stall mass was 62.5% of the engine speed. Compared with the speed of the stall mass was 67.08% in the experiment, the numerical calculations effectively proved the accuracy of this numerical calculation method. The results of the numerical calculation are completely consistent with the experimental results, which indicates that the numerical calculation method is effective and can be used to predict the flow field distribution.

To delve deeper into the reasons behind this difference, since the main causes of stall are the leading edge spillage and trailing edge backflow of the gap leakage flow, the leakage vortex at the tip gap of the compressor moving blade is analyzed for the six operating conditions between operating condition 1 and operating condition 2 (the six operating conditions are selected as shown in Fig. 24).

First, the Q criterion is used to analyze the W_{xyz} parameters of the fluid located at a distance greater than 1e-5m from the wall, and the vortex cores are extracted. Figure 25 illustrates the distribution of the extracted vortex cores at six distinct time instants within the tip clearance of the moving blade.

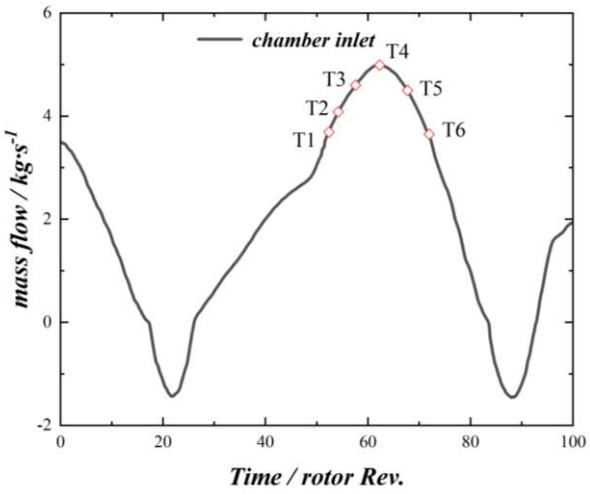

Fig. 24 Selection of operating points T1 to T6

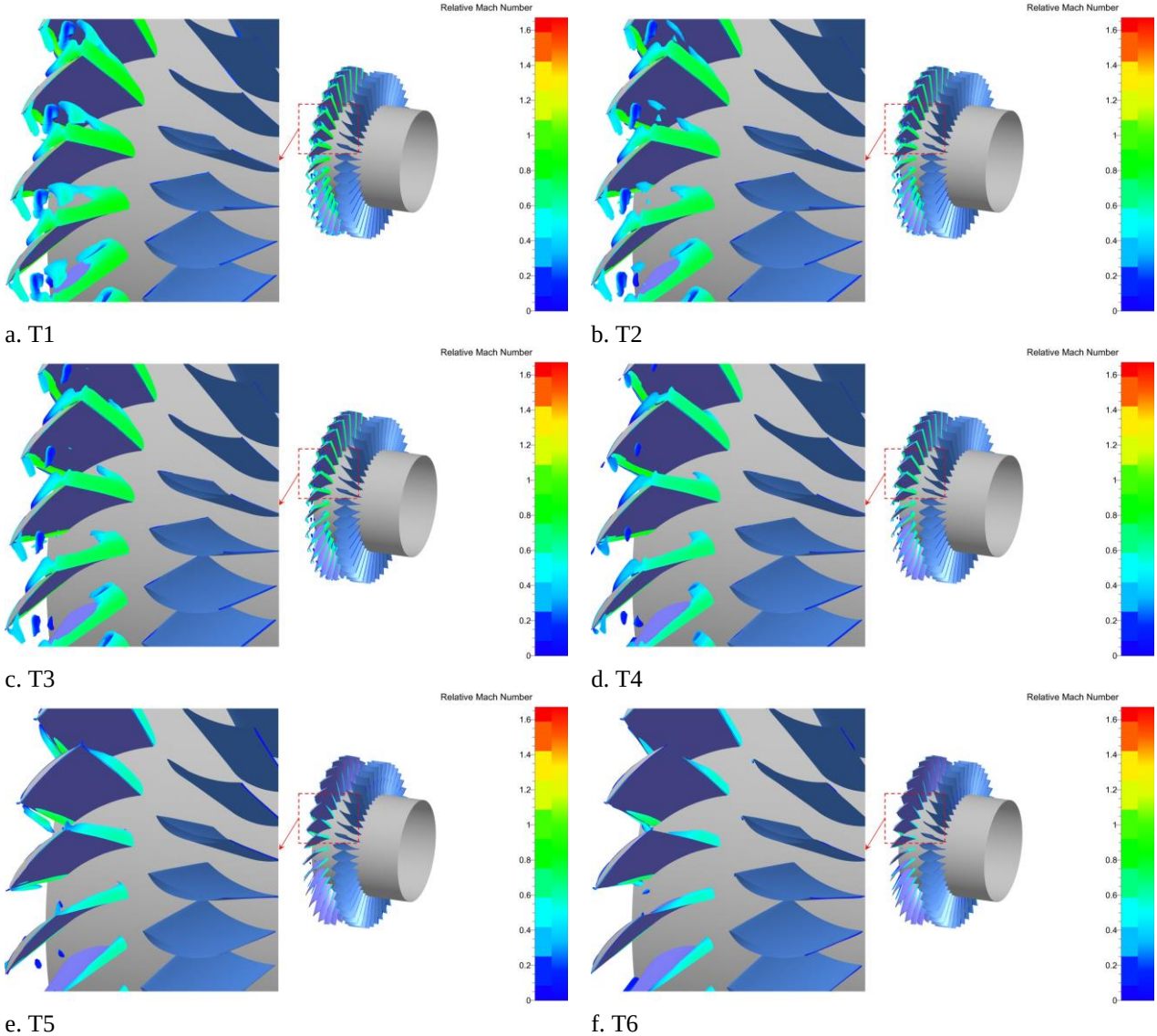

Fig. 25 Vortex cores of the gap leakage at different times

Figure 25 depicts the evolution of the vortex cores at the blade tip gap. As the stall process transits from the forward recovery *(CD)* to the chamber recovery stage *(DE)*, the vortex core structures undergo significant changes.

Within the stall region, the vortex cores appear significantly larger, practically occupying the entire passage. Additionally, these vortex core structures are unstable, which could be a contributing factor to the stall phenomenon itself.

As the stall process advanced to the chamber recovery stage, the shear forces and viscous dissipation within the flow field gradually increased. These effects lead to the stretching and fragmentation of the vortex structures, ultimately causing them to disappear.

Consequently, with the dissipation of the vortex, the rotating stall phenomenon also ceases to exist. This allows the flow distribution within the channels to return to a uniform state.

4. CONCLUSIONS

This paper utilizes a full-annulus numerical calculation method to investigate the phenomenon of deep stall phenomenon in axis compressors. The system-level macro-dynamic characteristics of the stall cycle process and the mechanism of the influence of surge on the stall characteristics are analyzed.

1. The specific conclusions are as follows: The deep stall cycle process was simulated using Riemann Invariant boundary conditions. The results showed that the compressor system experienced four stages during a surge cycle: Forward deceleration, Reverse backflow, Forward recovery, and Chamber recovery. During the stall process, the inlet and outlet mass flow and pressure rise of the system all exhibited low-frequency large-amplitude oscillation phenomena. The maximum forward mass flow rate can reach 4.98kg/s, while the maximum reverse mass flow rate reaches -1.46kg/s.
2. The transient pressure rise behavior within the compressor chamber exhibits a counter-clockwise hysteresis loop. This implies that during the decrease in mass flow rate, the pressure rise experienced by the chamber surpasses the compressor itself. Conversely, when the mass flow rate increases, the chamber pressure rise is less than the compressor pressure rise. The magnitude of this difference between the two pressure rises dictates the rate of flow fluctuation within the system.
3. The flow oscillation during the stall process play a role in the development of stall disturbances. Two distinct operating conditions are of particular interest: one is located in the forward recovery region and the other is located in the chamber recovery region. The former will promote the development of stall disturbances in the compressor, while the latter will suppress the development of stall disturbances. The underlying reason is that the flow field under different operating conditions will produce different shear effects and viscous dissipation on the fluid in the channel, which in turn has a contrasting impact on the stall phenomenon.

ACKNOWLEDGEMENTS

Research funding: The authors thank for The support of the Major Science and Technology Project of China No. Y2022-II-0002-0005.

CONFLICTS OF INTERESTS:

No conflict of interest

AUTHORS' CONTRIBUTIONS:

Y. Qiao: Conceived the innovative points of the paper and was responsible for the writing. **W. Chu:** Provided financial support and consultation. **H. Zhang:** Offered technical support. **K. Wang:** Proofread the manuscript. **X. Yang:** Assisted in conducting the experiments.

REFERENCES

Amulfi, G. L., Massardo, A. F., Giannattasio, P., Michell, D., Giusto, C., & Pinamonti, P. (1998). Multistage centrifugal compressor surge analysis part i: experimental investigation. *Journal of Turbomachinery*, *121*(2), 305–311. https://doi.org/10.1115/1.2841316

Arroyo, C. P., Dombard, J., Duchaine, F., Gicquel, L., Martin, B., Odier, N., & Staffelbach, G. (2021). Towards the large-eddy simulation of a full engine: Integration of a 360 azimuthal degrees fan, compressor and combustion chamber. Part I: Methodology and initialisation. *Journal Of The Global Power And Propulsion Society*. https://doi.org/10.33737/jgpps/133115

Bitikofer, C., Schoen, M. P., Li, J., & Lin, F. (2017). *Characteristic Moore-Greitzer Model Parameter Identification for a one stage Axial Compressor System*. https://doi.org/10.23919/ACC.2017.7962948

Courtiade, N., & Ottavy, X. (2013). Experimental study of surge precursors in a high-speed multistage compressor. *Journal Of Turbomachinery-Transactions Of The Asme*, *135*(6) . https://doi.org/10.1115/1.4023462

Crevel, F., Gourdain, N., & Ottavy, X. (2014). Numerical simulation of aerodynamic instabilities in a multistage high-speed high-pressure compressor on its test rig-part ii: deep surge. *Journal of Turbomachinery-Transactions of the Asme*,*136*(10). https://doi.org/10.1115/1.4027968

Faltin, Z., & Beneda, K. (2024). Combined numerical and experimental investigation of a centrifugal compressor with surge supression holes at the impeller hub. *Acta Polytechnica Hungarica*, *21*(8). https://acta.uni-obuda.hu/Faltin_Beneda_148.pdf

Greitzer, E. M. (1976a). Surge and rotating stall in axial-flow compressors.2. experimental results and comparison with theory. *Journal of Engineering for Power-Transactions of the Asme*, *98*(2), 199–217. https://doi.org/10.1115/1.3446139

Greitzer, E. M. (1976b). Surge and rotating stall in axial-flow compressors .1. theoretical compression system model. *Journal of Engineering for Power-Transactions of the Asme*, *98*(2), 190–198. https://doi.org/10.1115/1.3446138

Greitzer, E. M. (2009). Some aerodynamic problems of aircraft engines: fifty years after -the 2007 igti scholar lecture. *Journal of Turbomachinery-Transactions of the Asme*, *131*(3). https://doi.org/10.1115/1.2992515

Guo, Z., Chu, W., Zhang, H., & Liu, K. (2024). An efficient sparse surrogate model for aerodynamic characteristics of a supersonic compressor cascade with uncertain geometric deformations. *Aerospace Science and Technology*, *150*. https://doi.org/10.1016/j.ast.2024.109133

Guo, Z., Chu, W., Zhang, H., Liang, C., & Meng, D. (2023). Statistical evaluation of stability margin of a multi-stage compressor with geometric variability using adaptive polynomial chaos-Kriging model. *Physics of Fluids*, *35*(7), 076114. https://doi.org/10.1063/5.0158821

Hou, Y., Wang, Y., Pan, Y., He, W., Huang, W., Wu, P., & Wu, D. (2022). Vibration-based early surge detection and diagnosis of the centrifugal compressor using adaptive feature fusion and sparse ensemble learning approach. *SSRN Electronic Journal*. https://doi.org/10.1016/j.aei.2023.101947

Langston, L. S. (2017). Stall and surge are endemic scourges of jet engine and gas turbine operation. *Mechanical Engineering*, *139*(4), 36–41. https://doi.org/10.1115/1.2017-Apr-2

Lee, K. B., Dodds, J., Wilson, M., & Vahdati, M. (2018). Validation of a Numerical model for predicting stalled flows in a low-speed fan-part II: Unsteady analysis. *Journal of Turbomachinery-Transactions of the Asme*, *140*(5). https://doi.org/10.1115/1.4039052

Liu, X., Zhou, Y., Sun, X., & Sun, D. (2015). Calculation of flow instability inception in high speed axial compressors based on an eigenvalue theory. *Journal of Turbomachinery-Transactions of the Asme*, *137*(6). https://doi.org/10.1115/1.4028768

Munari, E., Morini, M., Pinelli, M., Brun, K., Simons, S., & Kurz, R. (2019). A new index to evaluate the potential damage of a surge event: the surge severity coefficient. *Journal of Engineering For Gas Turbines and Power-Transactions of the Asme*, *141*(3). https://doi.org/10.1115/1.4041255

Righi, M., Pachidis, V., Konozsy, L., Zhao, F., & Vahdati, M. (2020). Three-dimensional low-order surge model for high-speed axial compressors. *Journal of the Global Power and Propulsion Society*, *4*. https://doi.org/10.33737/jgpps/130790

Schoenenborn, H., & de Vries, M. (2013). Aeroelasticity at reversed flow conditions-part III: reduction of surge loads by means of intentional mistuning. *Journal of Turbomachinery-Transactions of the Asme*, *135*(4). https://doi.org/10.1115/1.4007683

Shahriyari, M. J., Firouzabadi, A., Khaleghi, H., & Esmailifar, S. M. (2024). A new model for compressor surge and stall control. *Scientific Reports*, *14*(1), 5347. https://www.nature.com/articles/s41598-024-55816-w

Sheng, H., Chen, Q., Li, J., Li, Z., Wang, Z., & Zhang, T. (2020). Robust adaptive backstepping active control of compressor surge based on wavelet neural network. *Aerospace Science and Technology*, *106*, 106139. https://doi.org/10.1016/j.ast.2020.106139

Wang, M., Sun, H., Wang, Z., Wang, Y., Magagnato, F., & Luan, Y. (2020). Numerical investigation of the effects of system volume and average mass flow on the surge characteristics of an axial compressor. *Aerospace Science and Technology*, *106*. https://doi.org/10.1016/j.ast.2020.106172

Xu, Y., Gu, H., Sun, J., Zhang, J., & Imani, H. (2024). Surge and stall instabilities finite-time control of nonlinear uncertain-disturbed compression system by using a novel robust approach. *Automatika*, *65*(3), 1050–1060. https://doi.org/10.1080/00051144.2024.2329503

Yi, Y., & Sun, M. (2024). Research and simulation of fuzzy expert anti-surge control system for compressor. *Frontiers in Computing and Intelligent Systems*, *7*(1), 1–5. https://drpress.org/ojs/index.php/fcis/article/view/16170

Zhang, H., Yang, Y., Xu, C., Hong, S., & Huang, G. (2024). Numerical study of the coherent characteristics of the blade tip of a micro centrifugal compressor and its application in a new unsteady casing-treatment experiment. *Physics of Fluids*, *36*(1). https://doi.org/10.1063/5.0190152

Zhao, F., Dodds, J., & Vahdati, M. (2021). Flow physics during surge and recovery of a multi-stage high-speed compressor. *Journal of Turbomachinery-Transactions of the Asme*, *143*(6). https://doi.org/10.1115/1.4050240

Zheng, D., Tang, X., Wu, X., Zhang, K., Lu, C., & Tian, L. (2021). Surge fault detection of aeroengines based on fusion neural network. *Intelligent Automation & Soft Computing*, *29*(3), 815–826. https://doi.org/10.32604/iasc.2021.017737